








# Multi-Band Photonic Integrated Wavelength Selective Switch

Rafael Kraemer , Fumi Nakamura , *Member, IEEE*, Menno van den Hout , *Graduate Student Member, IEEE*, Sjoerd van der Heide , *Graduate Student Member, IEEE*, Chigo Okonkwo , *Senior Member, IEEE*, Hiroyuki Tsuda, *Member, IEEE*, Antonio Napoli , and Nicola Calabretta 

**Abstract**—As fiber-optic systems turn toward multi-band transmission (MBT), exploiting the complete low loss window of optical fibers, novel optical components, able to operate in bands other than the conventional C-band, become necessary. In light of this, we report on a multi-band photonic integrated  $1 \times 2$  wavelength selective switch (WSS) operating in the O, S, C and L-bands. The photonic integrated WSS presented in this work uses a folded arrayed-waveguide grating (AWG) as the filtering element, while the wideband operation of the thermo-optic switches allows the routing of the individual channels from those bands to any of the device output ports. The operation of the WSS is experimentally validated for different bands and modulation formats. Results show error-free operation with limited penalty with intensity-modulation direct-detection (IM/DD) non-return-to-zero on-off keying (NRZ-OOK) up to 35 Gb/s in O, S, C and L-bands and up to 169.83 Gb/s with coherent 64-quadrature amplitude modulation (QAM) data transmission in the S, C and L-bands.

**Index Terms**—Wideband, multi-band, Coherent, Wavelength selective switch, Photonics.

## I. INTRODUCTION

IP data traffic demand for metro and data center interconnects (DCIs) is predicted to continue its exponential yearly growth for the foreseeable future [1]. There are several possible approaches to boost the transmission capacity in optical systems such as space-division multiplexing (SDM), multi-mode fiber (MMF), multi-core fiber (MCF) or multi-band transmission (MBT) [2]. Among them MBT has gathered special attention. Numerical studies suggest that MBT systems may provide up to a 10 fold increase in capacity when compared to C-band

systems only [2], [3]. This is achieved by utilizing the entire low loss spectrum of optical fibers, from 1260 nm to 1625 nm (O  $\rightarrow$  L-band). MBT systems are already being deployed as C+L [4], [5], by capitalizing on the re-use of erbium-doped fiber amplifiers (EDFAs) also within the L-band. More recently, S+C+L-band systems started being subject of active research, from numerical studies [3], [6] that showed the potential of these three-band systems to triple the capacity when compared against C-band only, to experimental setups employing power optimization schemes [5], wideband semiconductor optical amplifiers (SOAs) [7], [8] and continuous bandwidth amplification and geometric shaping for record breaking data transmission [9]. As MBT systems gain commercial traction, solutions for, e.g., spectrum management and routing are required. In this context, multi-band wavelength selective switch (WSS) is one of the main network elements. High port-count, flexible grid WSSs finds its use in the metro-core and transport segments of optical networks while in metro-access networks with converged 5 G distribution, where it is predicted a large deployment of nodes, a low-cost fixed grid solution for optical add-drop multiplexers (OADMs) is currently preferred. Such a solution is shown in Fig. 1, where the WSS presented in this work is in a typical two-degree add-drop configuration with a band demultiplexer that separates the multiband wavelength-division multiplexing (WDM) signal before the  $1 \times 2$  WSS modules. At its output, a band multiplexer recombines the multiband WDM signals. Furthermore, photonic integration may allow a considerable reduction of costs thanks to its potential for mass production, ease of fabrication, and packaging that could translate into a cheaper option than LCOS devices.

A tunable Silicon Photonics WSS that required fine tuning to operate in the C or L-bands, has been demonstrated in [10]. Also, C+L-band WSS based on free-space optics and liquid crystal on silicon (LCOS) started to become commercially available [11], but, as stated before, it is potentially a solution more suitable for nodes with multi-degree connectivity and will have its appeal in other network segments such as Metro-core and long-haul. In our previous work [12] we reported a preliminary characterization of a photonic integrated circuit (PIC) WSS operating on the S, C, and L-bands with NRZ-OOK.

In this paper, we present a thorough characterization of the multi-band, packaged and pig-tailed  $1 \times 2$  WSS operating on the O, S, C and L-bands and with 10 Gb/s for all bands,

Manuscript received March 7, 2021; revised May 25, 2021 and July 2, 2021; accepted July 6, 2021. Date of publication July 9, 2021; date of current version October 4, 2021. This work was supported by the European Union's Horizon 2020 research, and innovation programme under the Marie Skłodowska-Curie Grant 814276. (*Corresponding author: Rafael Kraemer.*)

Rafael Kraemer, Menno van den Hout, Sjoerd van der Heide, Chigo Okonkwo, and Nicola Calabretta are with IPI-ECO Research Institute, Eindhoven University of Technology, Eindhoven, AJ 5612, The Netherlands (e-mail: r.magalhaes.gomes.kraemer@tue.nl; m.v.d.hout@tue.nl; s.p.v.d.heide@tue.nl; cokonkwo@tue.nl; N.Calabretta@tue.nl).

Fumi Nakamura and Hiroyuki Tsuda are with Tsuda Laboratory, Graduate School of Science and Technology, Keio University, Yokohama 223-8522, Japan (e-mail: f\_nakamura@tsud.elec.keio.ac.jp; tsuda@elec.keio.ac.jp).

Antonio Napoli is with Infinera, London WC1V 7HP, U.K. (e-mail: ANapoli@infinera.com).

Color versions of one or more figures in this article are available at <https://doi.org/10.1109/JLT.2021.3096045>.

Digital Object Identifier 10.1109/JLT.2021.3096045

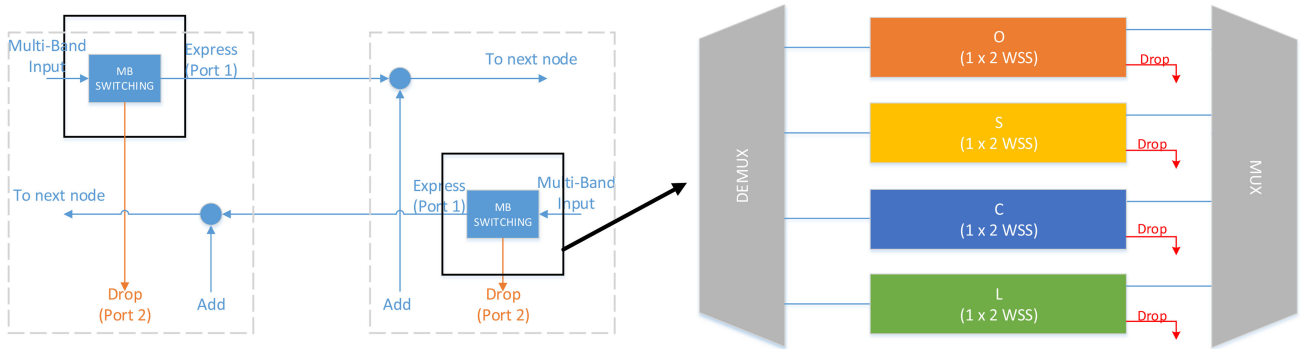


Fig. 1. Multi-band 2-degree switching node with band demultiplexer and multiplexer.  $1 \times 2$  multi-band wavelength selective switch (WSS) operating in the O, S, C and L-bands.

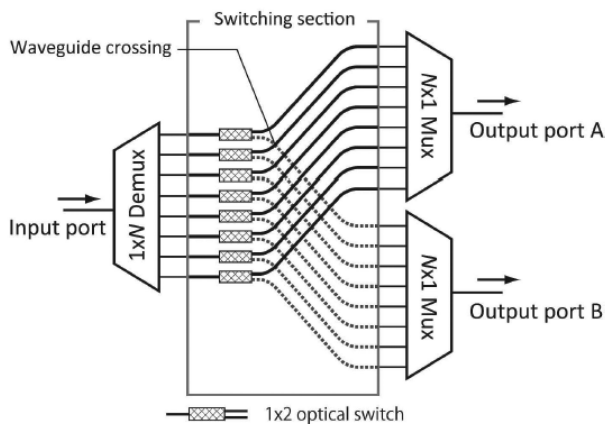


Fig. 2. A conventional WSS structure with 3 AWGs [13].

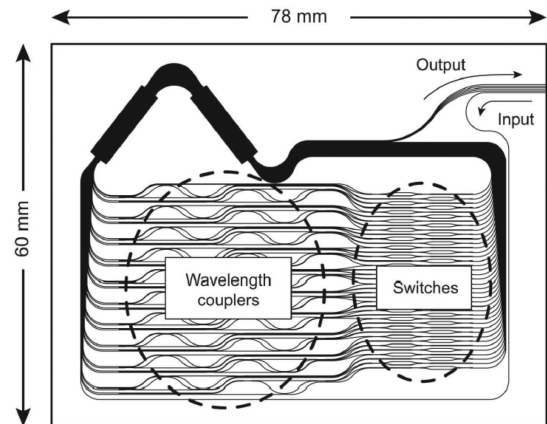


Fig. 3. Layout of the fabricated WSS [13].

35 Gb/s for the C and L-bands with NRZ-OOK data as well as multilevel modulation 33.3 GBd 64-quadrature amplitude modulation (QAM) coherent data transmission in the S, C and L-bands. From the individual channel transfer functions we also investigated the filtering and capacity reduction effect due to the cascade of multiple  $1 \times 2$  WSS based OADM nodes. Experimental results show error-free operation for all bands for the NRZ-OOK scenario with limited penalty, and below the forward error correction (FEC) threshold for 64-QAM data, which indicate that the PIC-WSS supports optical networks with variable modulation format.

## II. $1 \times 2$ PHOTONIC INTEGRATED WSS

The photonic integrated WSS is a one input two outputs ( $1 \times 2$ ) device, based on silica waveguides on a silicon substrate with a  $1.5\% \Delta$  contrast and designed for a channel spacing of 100 GHz in the C-band. In a conventional arrayed-waveguide gratings (AWGs) based  $1 \times 2$  WSS structure, as depicted in Fig. 2, the WDM light at the input is first separated into its individual channels by the first AWG, after that,  $1 \times 2$  optical switch gates directs the light to one of the two output ports where they are again recombined by two AWGs (one per output port) into WDM signals.

The fabricated device, as depicted in Fig. 3, uses unified arrayed-waveguide gratings (AWGs) in a loopback configuration for the demultiplexing and multiplexing section, reducing the AWG quantity from 3 to only 1. By doing that, potential mismatches between the center wavelengths of the AWGs are eliminated, while also contributing to reduce the device footprint. After the spatial separation of the individual channels, the wavelengths are directed to one of the two output ports by a switching section consisting of 40  $1 \times 2$  switches and  $2 \times 1$  wavelength couplers. The  $1 \times 2$  switches are a single-stage Mach-Zehnder interferometer (MZI) with two arms of equal length and a thermo-optic phase shifter. The wavelength couplers are based on an asymmetric type  $2 \times 1$  MZI which are composed of two arms with different lengths and 3-dB couplers, and it has the function of multiplexing adjacent channels. The heater for wavelength adjustment is on the top arm of each asymmetric MZI. The wavelength couplers contribute to reduce the size of the WSS by playing the role of merging adjacent channels toward Output 1 and Output 2 which loop back to the AWG for demultiplexing and multiplexing channels with a single structure. The wavelength couplers have a frequency response synchronized with the AWG, since the arms possess the same waveguide structure and the same group refractive index as the array waveguides. An embedded switch controller allows

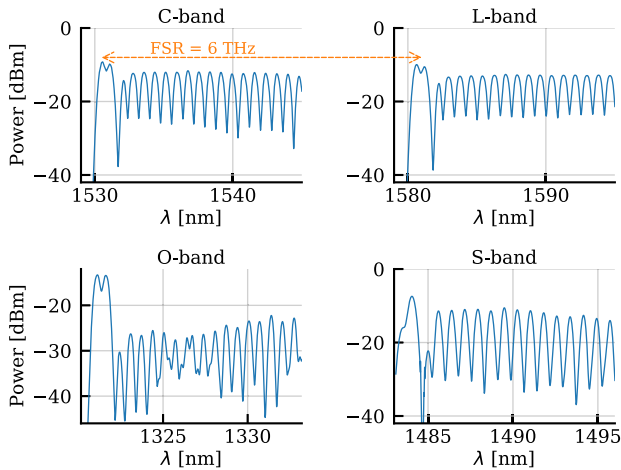


Fig. 4. Passband shape of the AWG.

the precise control of the heating current applied to each of the MZIs electrodes.

Since the transmission wavelengths of the AWG and the wavelength couplers are polarization sensitive, the WSS works for a single polarization. As stated in [13] the use of a silica substrate, which leads to the lower birefringence of the waveguides is a good solution to make the WSS polarization-insensitive. Scaling up the number of output ports is possible as we have already reported 100 GHz spacing 40 channels  $1 \times 4$  WSS using the same loopback configuration presented here [14]. Furthermore, increasing the number of channels is also possible by using larger relative refractive indexes,  $\Delta$ , as  $\Delta$ 's of 2% are already commercially available and  $\Delta$ 's of 5.5% were reported in [15].

#### A. Wideband Wavelength Separation – Filtering

The response of an AWG is periodical with the periodicity in the frequency domain being referred as the free-spectral-range (FSR) [16]. The 6THz FSR [13] of the fabricated AWG allows the periodic repetition of the passband across the spectrum. This periodicity on the fabricated device can be further verified from the spectrum in Fig. 4 where it is seen that the first channel of the L-band occurs after  $\sim 50$  nm of the first channel of the C-band. This means that channels from different optical bands have a fixed relationship. If we, for example, drop channel 1 in the O-band, the same channel 1 in the S, C and L-bands will be dropped as they propagate in the same output waveguide. While this means that a more careful wavelength plan is required across the multi-band spectrum, it also means that multiple wavelengths, across different FSRs can be dropped while switching only 1 channel.

From the passband shape, as seen in Fig. 4 we assessed average insertion losses (IL) of 23.80 dB, 11 dB, 12.70 dB and 13 dB in the O, S, C and L-band respectively. The maximum insertion losses were 27.6 dB, 16 dB, 15.60 dB, 13.80 dB and the minimum 22.15 dB, 7.76 dB, 9.20 dB, 9.90 dB across the O, S, C and L-band respectively. The extra insertion loss (IL) in the O-band comes from the wavelength couplers. This can be seen

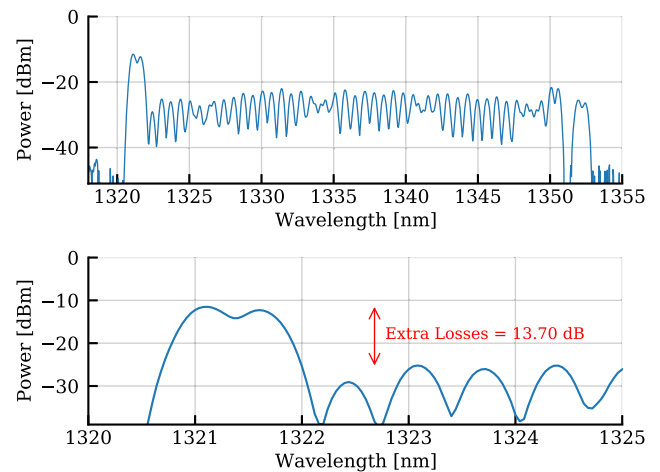


Fig. 5. Extra 13.7 dB losses in the O-band due to the wavelength couplers.

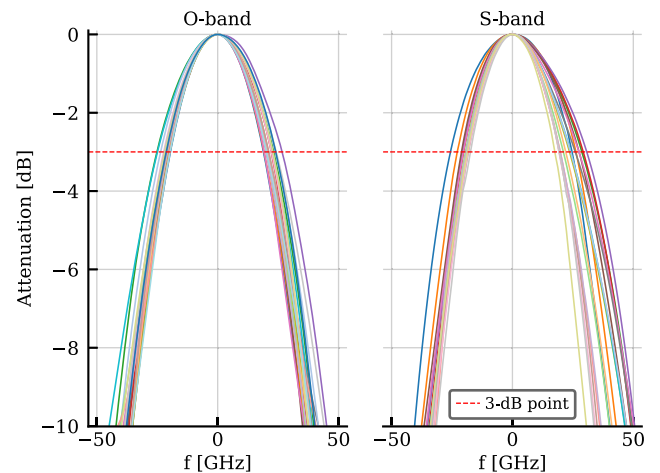


Fig. 6. Filter shape for the O and S-bands channels with average 3-dB bandwidths of 42.74 GHz and 43.48 GHz respectively.

from Fig. 5, where the loss of the channels which do not propagate through the wavelength couplers is around 13.7 dB smaller than the other wavelength channels, showing the wavelength dependence of the 3-dB couplers. The multi-band low loss WSS can be fabricated by adopting a phase generating couplers [17], which have been demonstrated to have broadband characteristics from the O- to the L-band, and four times lower losses when compared to conventional directional couplers, while providing low polarization dependent losses.

By extracting the individual channels of the WSS, as seen from Figs. 6 and 7, we could analyze the spectral performance across different bands, such as the 3 dB bandwidth, passband symmetry, and other possible imaging errors due to fabrication inaccuracies. From visual inspection of Figs. 6 and 7 we can verify that not all channels have an equal passband shape, and this asymmetry is greater when comparing channels in different bands.

As we have shown in Section II, the AWGs were designed for a channel spacing of 100 GHz in the C-band. In Fig. 9 we show the relative error from the designed 100 GHz spacing in the O, S, C and L-bands. The measured average channel spacing

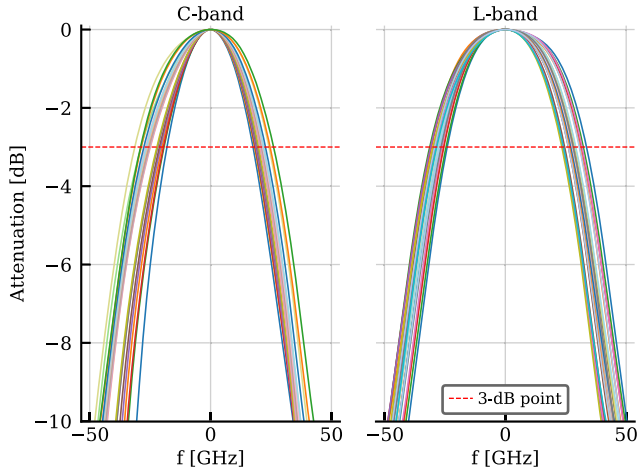


Fig. 7. Filter shape for the C and L-bands channels with average 3-dB bandwidths of 45.3 GHz and 54.36 GHz respectively.

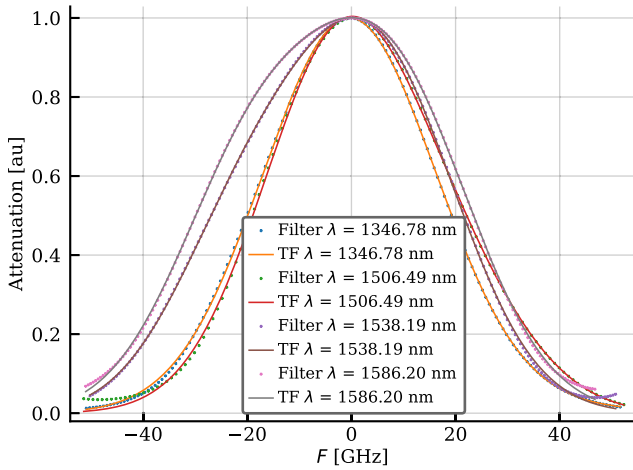


Fig. 8. Fit for calculating the AWG channels 3 dB bandwidth.

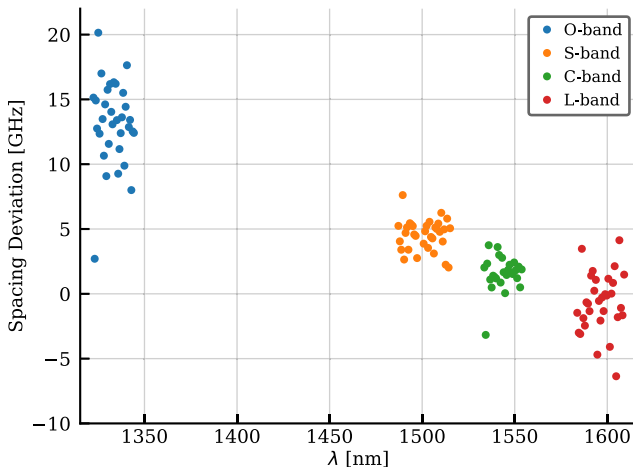


Fig. 9. Error in channel spacing when compared to a 100 GHz spaced grid across the O-, S-, C- and L-bands.

was 113.2 GHz, 104.8 GHz, 101 GHz and 99.3 GHz in the O, S, C and L-bands respectively. This arises from the group index dependency of the FSR [16], and consequently, as seen from the error in Fig. 9, is more accentuated as we move further away from the designed center frequency.

As stated in [18] the commonly used single Gaussian fit for modelling AWGs passband only partially reproduces the output real transfer function, because the decaying exponential nature of the real mode is underestimated by this approximation, and is shown that the real mode is better approximated by the sum of three Gaussian functions composed of different parameters representing the Input waveguides, array waveguides and the output waveguides of the AWG. We found that by approximating the passband shape by the sum of two Gaussian functions provided a good fit for the actual real mode as seen as can be verified in Fig. 8. From this computed transfer function we were able to numerically assess average 3 dB bandwidths of 42.74 GHz, 43.48 GHz, 45.3 GHz, 54.36 GHz in the O, S, C and L-bands respectively.

As seen in [16], the L-dB bandwidth of an AWG is given by:

$$\Delta f_L = 0.77 \frac{\omega_e}{d_r} \Delta f_{ch} \sqrt{L} \quad (1)$$

where  $d_r$  is the spacing between receiver waveguides,  $\Delta f_{ch}$  the channel spacing and  $\omega_e$  the waveguide mode effective width that is approximately given by [16]:

$$w_e \approx w_{wg} \left( 0.5 + \frac{1}{V - 0.6} \right) \quad (2)$$

in which  $w_{wg}$  is the waveguide width, and in [18] the 3 dB bandwidth,  $\Delta V_{bw}$ , is formulated as:

$$\Delta V_{bw} = 2\gamma\omega_e \sqrt{2 \ln 10^{3/10}} \quad (3)$$

where  $\gamma$  is the frequency spatial dispersion parameter. From (1) and (3) we find that the AWG 3 dB bandwidth decreases as the mode radius,  $\omega_e$  decreases, which in turn, as seen in (2), is smaller at higher frequencies, showing why the passband is narrower as we go to shorter wavelengths.

## B. Wideband Switching

As stated in Section I, the WSS makes use of the thermo-optic phase shifters on MZIs for the switching of individual wavelengths between the two output ports. In [19], [20], the Sellmeier relation was used to find the thermo-optic coefficient (TOC) of Silica glasses for a wide range of optical wavelengths and it was verified the low variability of these coefficients over a broad wavelength range, from 1260 nm to 1625 nm.  $2n(dn/dt)[10^{-6}/^\circ\text{C}]$  varied by less than 1% over this range for various optical Silicate Fiber Glasses. These results indicate that thermo-optic switching elements are very good option for wideband WSS.

Fig. 10 shows the spectrum at output Port 1 of the WSS at both switch states for the O, S, C and L-bands. The power ratio between the two output states is here defined as extinction-ratio (ER). We measured average ERs of 23.6 dB, 18.2 dB, 22.5 dB, 19.3 dB across the O, S, C and L-bands respectively. In Table I the average, the minimum and the maximum ERs for each band



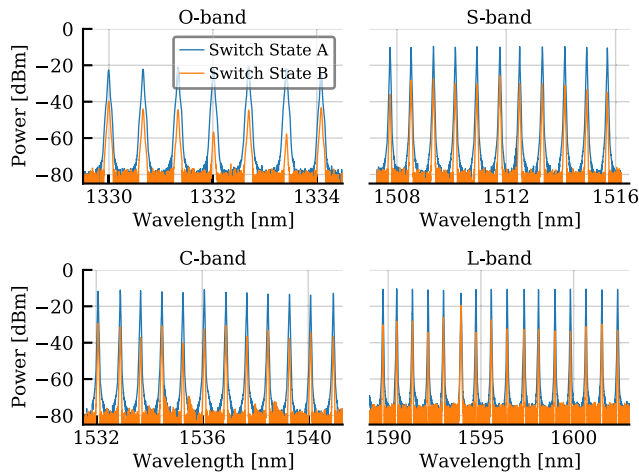


Fig. 10. Channels with an average ER of 23.6 dB, 18.2 dB, 22.5 dB, 19.3 dB in the O, S, C and L-bands respectively.

TABLE I  
EXTINCTION RATIO DATA FOR THE O, S, C AND L-BANDS

Band	Average ER	Minimum ER	Maximum ER
O-band	23.62 dB	11.94 dB	35.87 dB
S-band	18.21 dB	6.16 dB	37.59 dB
C-band	22.59 dB	14.77 dB	37.80 dB
L-band	19.38 dB	4.18 dB	26.22 dB

are shown. As seen from this table, the minimum ER is smaller than 15 dB the maximum ER is up to 37.8 dB. This variability will impact the system performance when wavelength channels are dropped and added in the same wavelength at the same time. Improving the ER is possible by using double Mach-Zehnder thermo-optic switches that have been shown to provide ERs between 49 dB to 76 dB with an average value of 60 dB [21], values that are high enough to overcome any in-band crosstalk induced limitation.

### III. EXPERIMENTAL DATA TRANSMISSION

To verify the possible penalties introduced by a single WSS, two experimental scenarios were considered. First, in Section III-A the WSS was tested with intensity-modulation direct-detection (IM/DD) format, which is currently employed in metro access nodes with edge computing [22]. In Section III-C the WSS was tested in a coherent transmission setup, where it could be employed in future high-capacity multi-band nodes where there is less need for multi-degree connectivity.

#### A. IM/DD Experimental Setup

The experimental setup that was employed to assess the performance of the WSS is depicted in Fig. 11. For the C and L-bands, a broadband tunable laser-source (TLS), covering both bands was used as a continuous-wave (CW) light source. After the CW source, a polarization controller (PC) was used to optimize the state of polarisation (SOP) for the Mach-Zehnder modulator (MZM), which was driven at 10 Gb/s and 35 Gb/s

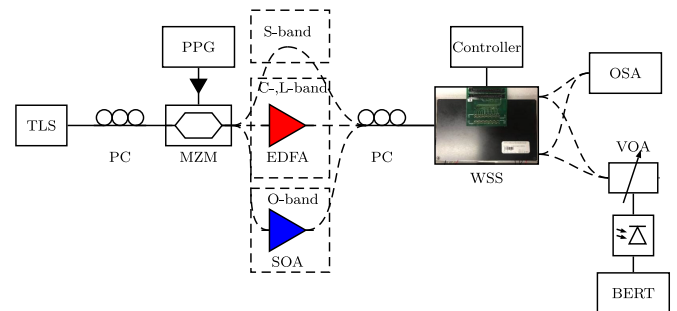


Fig. 11. NRZ-OOK Experimental setup. Tunable laser source (TLS), erbium-doped fiber amplifier (EDFA), polarization controller (PC), Mach-Zehnder modulator (MZM), variable optical attenuator (VOA), pulsed-pattern generator (PPG), optical spectrum analyzer (OSA), semiconductor optical amplifier (SOA).

(in the case of the C and L-bands) NRZ-OOK with a pseudorandom bit sequence (PRBS) length of  $2^{31} - 1$ . After the MZM, an EDFA was used to compensate for the modulator losses and another PC was used to optimize the SOP for the WSS. Following the WSS, a variable optical attenuator (VOA) was used for the power sweep, an optical spectrum analyzer (OSA) for spectral analysis and the optical signal-to-noise ratio (OSNR) of the signal and a photodetector (PD) to convert the signal from the optical to the electrical domain. For the O-band the same setup applies with some components being exchanged by the O-band counterpart, as for example, the CW source and the modulator. In the case of the EDFA it was substituted by an SOA and the PD was exchanged by a high sensitivity avalanche photodetector (APD) due to the higher IL in the O-band, which in turn limited the maximum data rate of the O-band experiments to 10 Gb/s. In the case of the S-band, as at the time we lacked amplifiers in this band, the APD was also employed, and as in the case of the O-band, limited the maximum data-rate for the S-band experiments to 10 Gb/s. Despite this the WSS is able to operate in these bands at 35 Gb/s with an expected increase in the penalties in the both bands due to the higher OSNR requirements at this data-rate and also because of the additional IL in the O-band which in turn also impacted the OSNR.

#### B. IM/DD Experimental Results

In Fig. 12 the bit error rate (BER) results at 10 Gb/s for the O and S-band is shown. In the case of the O-band, at  $\text{BER} = 10^{-9}$ , we could verify a maximum penalty at  $\lambda = 1300.06$  nm of 3.2 dB whereas in the S-band the maximum power penalty was at most 0.8 dB. From Fig. 12 we can also see the different power requirements for error free transmission in the O and S-band, on average  $-23$  dBm in the first case and around  $-28$  dBm in the second case. This, as discussed in Section III-A, is due to the lower OSNR in the O-band because of the higher IL and the use of the SOA that further degraded the OSNR.

For the case of the C and L-band, the obtained results are depicted in Fig. 13, not all tested channels in the C-band are shown for the easier interpretation of the figure, but have results that follow a similar trend to the ones present in the figure. The

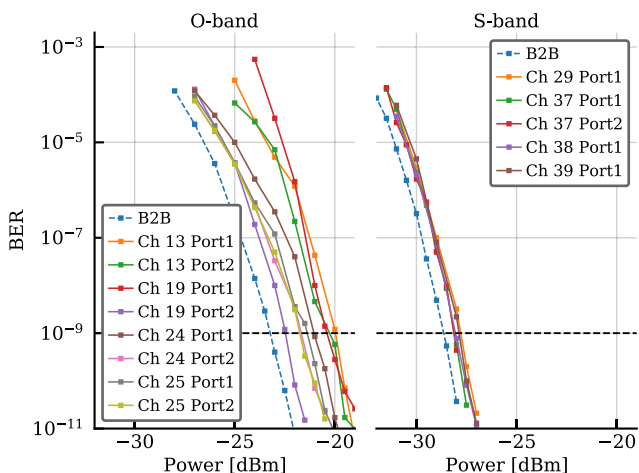


Fig. 12. Bit error rate results with 10 Gb/s NRZ-OOK data for the O and S-band.

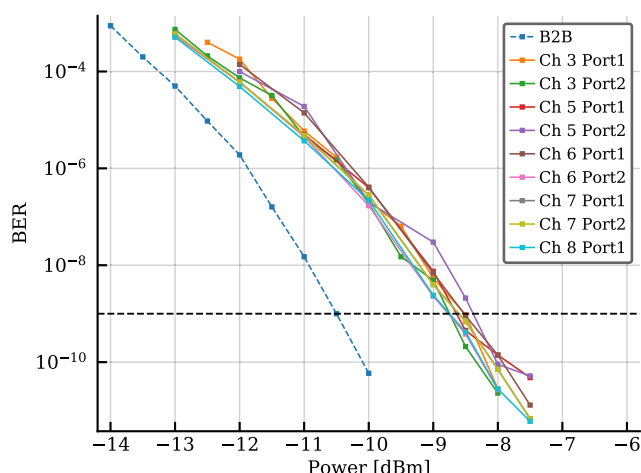


Fig. 14. BER results with 35 Gb/s NRZ-OOK data in the C-band.

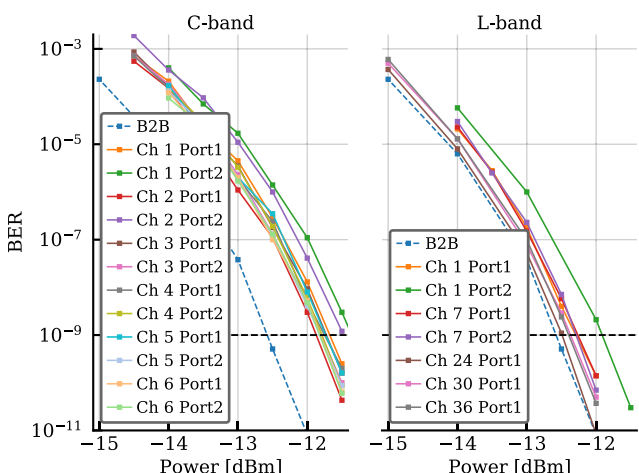


Fig. 13. Bit error rate results with 10 Gb/s NRZ-OOK data for the C and L-band.

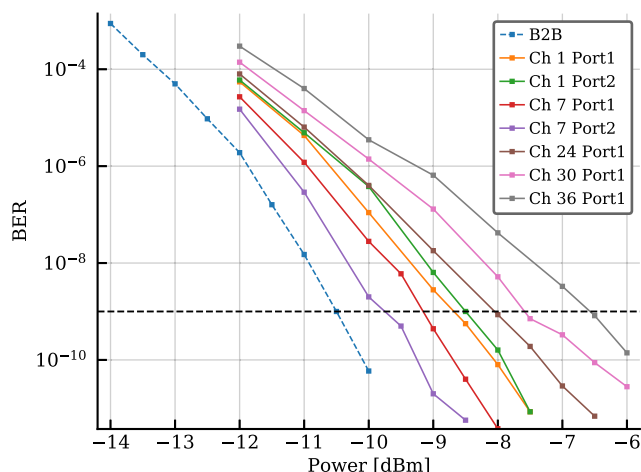


Fig. 15. BER results with 35 Gb/s NRZ-OOK data in the L-band.

penalties ranged from 0.2 dB to 1.1 dB. Similar performance was verified in the case of the L-band, with penalties ranging from 0.1 dB to 0.7 dB where the channels tested ranged from 1582.22 nm to 1610.72 nm.

In the results shown in Fig. 14 and 15, the C and L-band channels were tested at 35 Gb/s. In the case of the C-band the penalty was 2 dB at  $BER = 10^{-9}$  for most of the tested channels, and in the case of the L-band the penalty ranged from 0.7 dB to 3.5 dB. This difference in the reported penalties arises from slightly variations between the AWG channel shapes and deviations from the 100 GHz channel spacing, greater in the L-band as seen in Fig. 9, that introduce extra penalties to the signal.

To evaluate the possible penalty induced with more than 1 channel, 3 channels were loaded with NRZ-OOK data at 10 Gb/s in the C-band, with  $\lambda_1 = 1533.59$  nm,  $\lambda_2 = 1534.37$  nm and  $\lambda_3 = 1535.28$  nm. The modulated spectrum at 10 Gb/s is shown in Fig. 16. In the same figure we can verify the spectrum when only the channel at  $\lambda_1 = 1533.59$  nm is at port 1, with  $\lambda_2$  and  $\lambda_3$

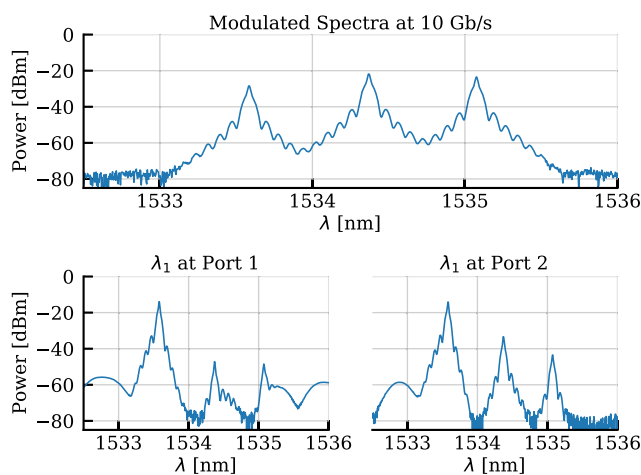


Fig. 16. Modulated spectra for 3 channels in the C-band with a single channel being switched between output ports 1 and 2.

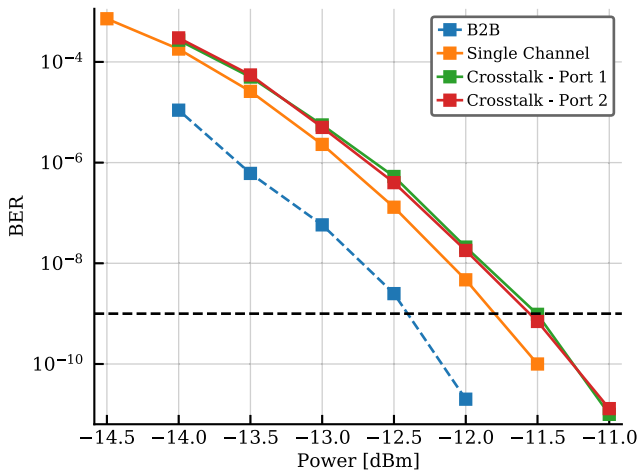


Fig. 17. Crosstalk induced penalty at 10 Gb/s for  $\lambda_1 = 1533.59$  nm.

switched to port 2, and when only the same channel is switched to port 2. The BER results for both scenarios are shown in Fig. 17 and compared to the previously reported BER from Fig. 13. We verified at each port a penalty of around 1 dB, an increase of 0.3 dB when compared to the single loaded channel case. This shows that at least a single drop-stage could be realized without a substantial increase in the incurred penalties.

### C. Coherent Experimental Setup

To assess possible impairments introduced by the WSS in a coherent transmission, we used the experimental setup shown in the schematic depicted in Fig. 18. A tunable laser source (TLS) was set to wavelengths 1515.74 nm and 1516.54 nm on the S-band, from 1532.75 nm to 1553.75 nm with 0.8 nm spacing on the C-band and from 1583.71 nm to 1599.60 nm with also 0.8 nm on the L-band. After the TLS an EDFA was used to amplify the continuous wave (CW) light that will also be used as a local oscillator (LO) to the coherent receiver. When testing S-band channels, an optical band pass filter (OBPF) was used to filter the out-of-band amplified spontaneous emission (ASE) noise generated by the EDFA. Offline, a PCG64 pseudo-random data streams containing  $2^{16}$  QAM symbols are pulse-shaped using a root-raised-cosine (RRC) filter with roll-off  $\beta = 0.01$  and uploaded to a 100GSa/s digital-to-analog converter (DAC). The DAC outputs are connected to radio frequency (RF) amplifiers which in turn are connected to the in-phase and quadrature optical modulator (IQ-MOD). After the modulator, the signal is fed into the WSS, which is remotely controlled according to the channel being tested. The two outputs of the WSS are connected to a mechanical optical switch for quick selection of one of the two outputs. Another EDFA is used to compensate for the IL of the WSS. Due to the lack of O-band IQ modulators, the coherent experiments covered only the S, C and L-bands.

A noise loading stage consisting of S-band SOAs, C-band EDFAs or L-band EDFA, connected to a VOA, was used for the OSNR sweep. The coherent receiver consisted of the already mentioned LO, a 90-degree hybrid and 2 balanced photodiodes.

The detected electrical signal is digitized by an 80GSa/s analog-to-digital converter (ADC) and further processed by the offline receiver digital signal processing (DSP), consisting of matched filtering, multiple-input multiple-output (MIMO) equalization with in-loop blind phase search, and performance metric evaluation.

### D. Coherent Experimental Results

The WSS performance was evaluated with 64-QAM 33.3 GBd data while sweeping the OSNR from the minimum achievable level, limited by the maximum output power of the respective noise loading stage, to the maximum OSNR value, where most of the noise power was attenuated by a VOA.

The back-to-back 33.3 GBd 64-QAM signal is plotted against the WSS channels on the S, C and L-bands in Fig. 19. From this figure it can be seen that we were able to match the signal to the center wavelength of the AWG channels. In reality, some mismatch is expected to occur between the laser and the filters center wavelengths, further increasing the filtering effects discussed in Section IV. This mismatch is a possible source of impairment especially for the S-band due to the smaller 3 dB bandwidth of the AWG channels as seen from Section II-A and Fig. 8. In Fig. 20 we can compare the signal spectrum for the back-to-back scenario and after propagating through the WSS for all evaluated channels in the S, C, and L-bands. For all tested channels, a negligible deterioration on the signal shape is verified.

A quantified measurement of the multi-band performance is reported in Fig. 21. As a figure of merit, besides the pre FEC BER, we use the normalized generalized mutual information (NGMI), as it has been shown to provide consistent post FEC BER predictions across different conditions and modulation formats [23]. Considering the FEC overhead for LDPC codes concatenated with a staircase code [24], the NGMI of 0.88 and 0.92 shown in this figure corresponds to an overall rate of 0.81 and 0.85 respectively, meaning that for the gross data-rate of 199.80 Gb/s the net data-rates after FEC decoding will be 161.84 Gb/s and 169.83 Gb/s for the NGMI values of 0.88 and 0.92 respectively. The curves that we report represent the averaged values of all tested channels in each band. We have performed and reported the NGMI values obtained for the S, C, and L-bands and at both output ports.

Fig. 22 shows the comparison of the OSNR values for each WSS channel against its back-to-back counterparts. The results show that the OSNR penalty changes with wavelength and with the port being tested. In the tested channels at the C-band the OSNR penalty was always smaller than 1 dB and in some cases negligible at both output ports. For the L-band the penalty is greater than 1 dB for most of the tested channels, and the penalty increases as we switch to output port 2. This increase in the OSNR penalty is also verified in the S-band and we believe its mainly because of the smaller ER in these bands as shown in Section II-B, where the ER is 22.59 dB in the C-band versus 18.22 dB in the S-band and 19.38 dB in the L-band.

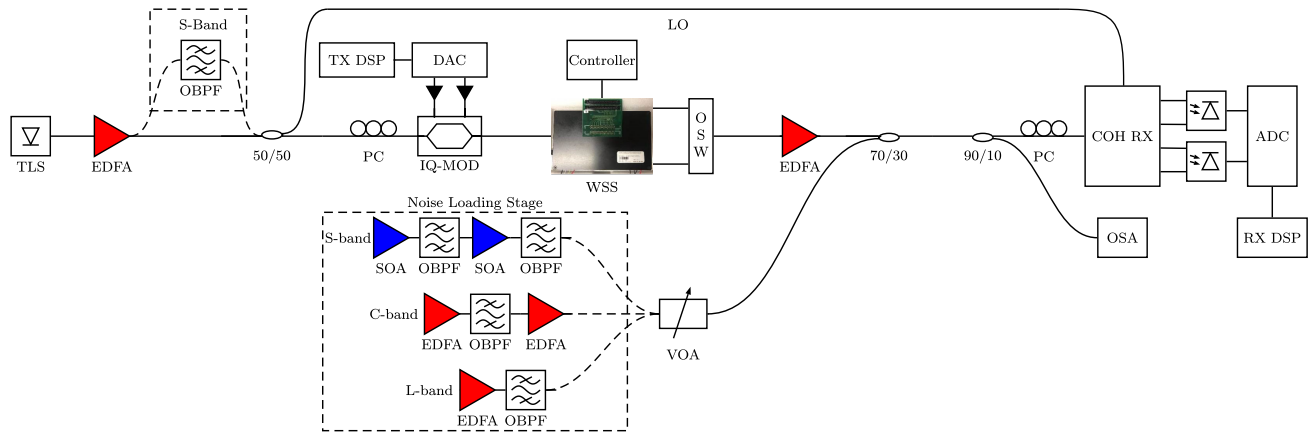


Fig. 18. Schematic of the experimental setup. Tunable laser source (TLS), erbium-doped fiber amplifier (EDFA), digital-to-analog converter (DAC), optical band pass filter (OBPF), polarization controller (PC), local oscillator (LO), in-phase and quadrature modulator (IQ-MOD), () digital signal processing (DSP), optical spectrum analyzer (OSA), analog-to-digital converter (ADC), semiconductor optical amplifier (SOA).

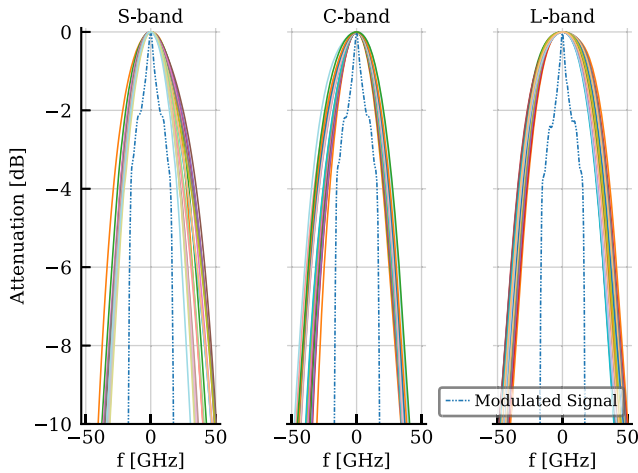


Fig. 19. The modulated 33.3 Gb/s signal on top of the individual channels on S-, C- and L-bands.

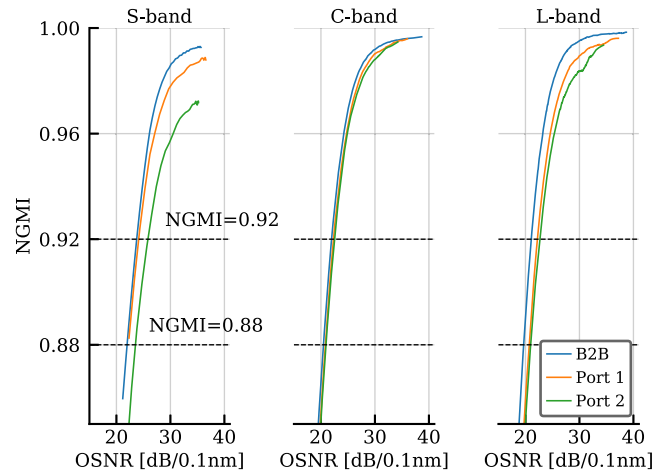


Fig. 21. Averaged NGMI and BER for the S,C and L-bands.

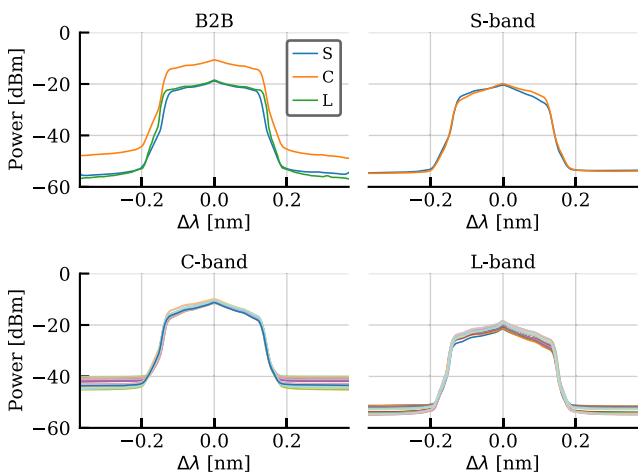


Fig. 20. 33.3 Gb/s modulated spectra at Back-to-Back and after passing through the WSS in the S, C and L-bands, for all tested channels.

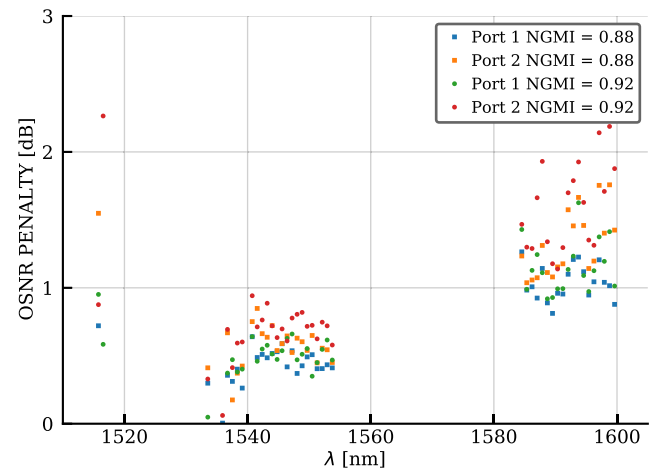


Fig. 22. OSNR penalty from the S to the L-band for NGMI values of 0.88 and 0.92, and corresponding net data-rates of 161.84 Gb/s and 169.83 Gb/s respectively.



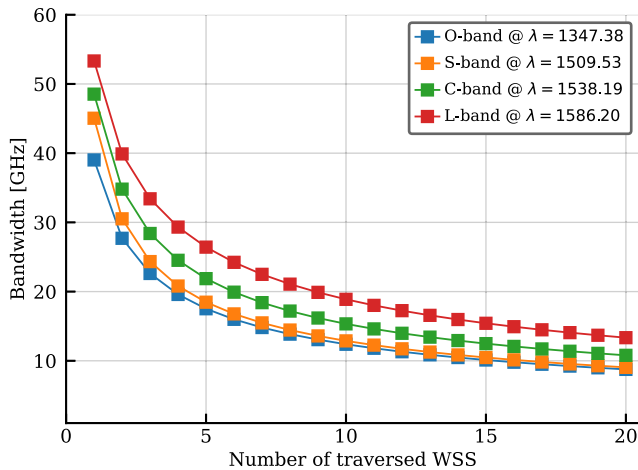


Fig. 23. 3 dB bandwidth reduction in function of the number of traversed WSS.

### E. Experimental Conclusions and Outlook

In this section, we assessed the penalties introduced by the WSS when loading channels across multiple optical bands and switching it between the two output ports. We achieved error free operation with limited penalty with NRZ-OOK data and below the FEC threshold for coherent 64-QAM. Results indicate that an optimized design with flat-top operation and double gates are important in order to reduce the bandwidth narrowing effect in cascaded WSSs as well as improving the ER. Moreover, further experimental validation from a network perspective are necessary, such as adding a channel on top of a dropped one and investigate the impact on the OSNR after the traversal of multiple WSSs based nodes for different modulation formats and data rates.

## IV. WSS BANDWIDTH NARROWING

Due to the filtering effects seen in Section II-A, we investigate the bandwidth narrowing after the traversal of several  $1 \times 2$  WSS based OADM nodes. In order to calculate the resulting 3 dB bandwidth after the cascade of several WSS, we used the computed transfer functions for different bands as shown in Section II-A.

The bandwidth narrowing effect was computed from 1 to 20 traversed  $1 \times 2$  WSS as the possible maximum number of cascaded nodes for metro-access networks where this device is most applicable. As the cascading of WSS devices has the net effect of multiplying the bandpass filter spectra together [25] we can calculate the resulting filter with the computed transfer function from the measured data.

In Fig. 23 we show the 3 dB bandwidth reduction as a function of the number of traversed WSS for selected channels in the O, S, C and L-bands. It was verified that, for the O and S-band, after 15 traversed WSS the bandwidth was already smaller than 10 GHz, potentially limiting this band for scenarios where the bandwidth requirements and/or the number of traversed filters is small. In the case of the C-band, after 20 traversed WSS the

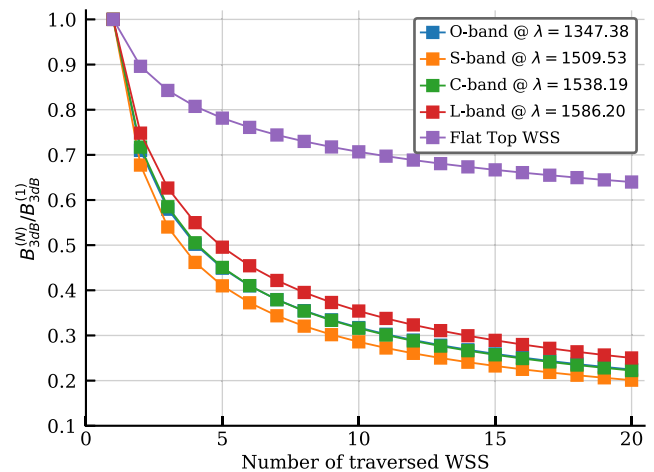


Fig. 24. Normalized 3 dB bandwidth reduction vs number of traversed WSS.

3 dB bandwidth was close to 10 GHz and around 15 GHz for the L-band.

By using a flat top WSS as shown in [25] we can potentially limit the bandwidth reduction after traversing several WSSs. It is expected that the filter narrowing effect would be much smaller than in the case for Gaussian shaped filter, as presented in this work. This is further confirmed in Fig. 24 where we show the normalized 3 dB bandwidth as a function of the number of traversed devices. We can see from this figure that the filter narrowing is much smaller than in the case of the device presented in this work. We verified that for the case of this WSS, after 20 traversed WSS the resulting 3 dB bandwidth is 20% of its original value, while for the flat top WSS the bandwidth was still greater than 60% of the original bandwidth. This shows that for traversing multiple devices with high-bandwidth signals, a flat-top passband is a must.

Another potential issue is the limited ER shown in Section II-B, that may induce additional penalties when adding a channel at the same wavelength of the dropped channel. Improving the ER to reduce the in-band crosstalk is possible by using the double-gate switches [21], [26] as discussed in Section II-B. Another solution revolves around adding 2 WSSs per node for the ER improvement, but would come with the cost of a more accentuated bandwidth reduction than the one seen in Fig. 24. In this case the 3 dB bandwidth would be around 30% of its original value after just 5 nodes and after 20 nodes close to only 10%.

Photonic integrated flat top WSSs are realizable by adjusting the spectral response of the AWGs. Several approaches are possible, such as the use of multimode waveguides at the receiver side [16], but is limited in application because it can only be applied on the receiver side where the multimode waveguides are directly coupled to a detector without additional signal loss. Flattening by the multigrating method [27] is another approach that is realized by using several interleaved sub-gratings of monomode waveguides getting a final response that is the addition of all the sub-responses, thus flattening the passband. It was reported that the 1 dB bandwidth more than doubled by using this approach when compared to conventional AWGs.

Another approach [28] based on nonuniform AWGs showed that the optimized nonuniform AWG had a flat passband with 1 dB and 3 dB bandwidths 2.3 times larger than conventional uniform AWGs.

## V. CONCLUSIONS

In this work, we experimentally demonstrated and assessed a photonic integrated WSS operating in the O, S, C, and L-bands. We have shown that the cyclic nature of the AWGs allows the selection of wavelength channels across multiple optical bands. Furthermore, we also showed that the wideband nature of the thermo-optic effect on Silica makes thermo-optic switches a relevant option for wideband WSSs.

Experimental data transmission showed error-free operation across all tested bands and channels, with a minimum power penalty of 0.2 dB in the C-band to a maximum power penalty of 3.2 dB in the O-band at 10 Gb/s. For 35 Gb/s the penalty was at its minimum 0.7 dB and at most 3.5 dB, both in the L-band with NRZ-OOK. In the 64-QAM coherent case, with a net data-rate of 169.83 Gb/s the OSNR penalty was smaller than 1 dB for all channels in the C-band and the maximum OSNR penalty was of 2.3 dB in the L-band.

We also point out that, due to the asymmetric and Gaussian, shape of the AWG passband, the 3 dB bandwidth reduction is more accentuated than reported in other studies that were based on flat-top devices. As described before, the implementation of photonic integrated WSSs with passband-flattened AWGs [27] is a way to prevent bandwidth narrowing and the number of possible traversed nodes, as it may more than double the 1 dB bandwidth [28]. Moreover, further improvement of the ER is possible by using double-gate thermo-optic switches [21] while maintaining the wideband nature of the switching element.

The considered PIC WSS with a single AWG serving multiple optical bands may reduce the costs associated with the deployment of multi-band optical add-drop nodes, by reducing chip size and component count. With a power equalization solution using VOAs, that were already successfully demonstrated in PLC PICs [29], this device architecture could be a viable and deployable solution for future multi-band low-degree optical add drop nodes.

## REFERENCES

- [1] "Cisco annual internet report - cisco annual internet report (2018.2023) white paper - cisco," [Online]. Available: <https://www.cisco.com/c/en/us/solutions/collateral/executive-perspectives/annual-internet-report/white-paper-c11-741490.html>
- [2] A. Ferrari *et al.*, "Assessment on the achievable throughput of multi-band ITU-T G.652.D fiber transmission systems," *J. Lightw. Technol.*, vol. 38, no. 16, pp. 4279–4291, 2020.
- [3] N. Sambo *et al.*, "Provisioning in multi-band optical networks," *J. Lightw. Technol.*, vol. 38, no. 9, pp. 2598–2605, 2020.
- [4] M. Cantono, R. Schmogrow, M. Newland, V. Vusirikala, and T. Hofmeister, "Opportunities and challenges of C+L transmission systems," *J. Lightw. Technol.*, vol. 38, no. 5, pp. 1050–1060, 2020.
- [5] J. Cai *et al.*, "70.4 tb/s capacity over 7600 km in C+L band using coded modulation with hybrid constellation shaping and nonlinearity compensation," in *Proc. Opt. Fiber Commun. Conf. Exhib.*, 2017, pp. 1–3.
- [6] B. Correia *et al.*, "Power control strategies and network performance assessment for C+L+S multiband optical transport," *J. Opt. Commun. Netw.*, vol. 13, no. 7, pp. 147–157, 07 2021.
- [7] F. Hamaoka *et al.*, "Ultra-wideband WDM transmission in S-, C-, and L-Bands using signal power optimization scheme," *J. Lightw. Technol.*, vol. 37, no. 8, pp. 1764–1771, 2019.
- [8] J. Renaudier *et al.*, "Recent advances in 100 nm ultra-wideband fiber-optic transmission systems using semiconductor optical amplifiers," *J. Lightw. Technol.*, vol. 38, no. 5, pp. 1071–1079, 2020.
- [9] L. Galdino *et al.*, "Optical fibre capacity optimisation via continuous bandwidth amplification and geometric shaping," *IEEE Photon. Technol. Lett.*, vol. 32, no. 17, pp. 1021–1024, Sep. 2020.
- [10] P. Prabhathan, Z. Jing, V. M. Murukeshan, Z. Huijuan, and C. Shiyi, "Discrete and fine wavelength tunable thermo-optic WSS for low power consumption C+L band tunability," *IEEE Photon. Technol. Lett.*, vol. 24, no. 2, pp. 152–154, Jan. 2012.
- [11] "Finisar WSS Dual Wavelength Selective Switch (WSS)." [Online]. Available: [https://finisarwss.com/wp-content/uploads/2020/07/FinisarWSS\\_Dual\\_Wavelength\\_Selective\\_Switch\\_ProductBrief\\_Jul2020.pdf](https://finisarwss.com/wp-content/uploads/2020/07/FinisarWSS_Dual_Wavelength_Selective_Switch_ProductBrief_Jul2020.pdf)
- [12] R. Kraemer, F. Nakamura, H. Tsuda, A. Napoli, and Calabretta, "S-, C- and L-Band photonic integrated wavelength selective switch," in *Proc. Eur. Conf. Opt. Commun.*, 2020, pp. 1–4.
- [13] Y. Ikuma, T. Mizuno, H. Takahashi, and H. Tsuda, "Integrated 40- $\lambda$ 1  $\times$  2 wavelength selective switch without waveguide crossings," *IEEE Photon. Technol. Lett.*, vol. 25, no. 6, pp. 531–534, Mar. 2013.
- [14] T. Yoshida, H. Asakura, H. Tsuda, T. Mizuno, and H. Takahashi, "Switching characteristics of a 100-GHz-spacing integrated 40- $\lambda$ 1  $\times$  4 wavelength selective switch," *IEEE Photon. Technol. Lett.*, vol. 26, no. 5, pp. 451–453, Mar. 2014.
- [15] M. Takahashiy, Y. Uchiday, and S. Yamasakiy *et al.*, "Development of lowloss ultra-high $\Delta$ ZrO<sub>2</sub>-SiO<sub>2</sub> PLC for next generation compact and high-density integrated devices," *IEICE Trans. Electron.*, vol. E97-C, no. 7, pp. 725–730, 2014, doi: [10.1587/transele.E97.C.725](https://doi.org/10.1587/transele.E97.C.725).
- [16] M. Smit and C. Van Dam, "PHASAR-based WDM-devices: Principles, design and applications," *IEEE J. Sel. Topics Quantum Electron.*, vol. 2, no. 2, pp. 236–250, Jun. 1996.
- [17] T. Watanabe, T. Mizuno, Y. Hashizume, and T. Takahashi, "Silica-Based Plc 1  $\times$  n Switch for All Wavelength Bands," in *Proc. Opt. Fiber Commun. Conf., Opt. Soc. Amer. (OSA)*, 2014, Paper Th11.5.
- [18] Z. Liu and J. Li, "Modeling and design of arrayed waveguide gratings," in *Proc. CAR 2010-2010 2nd Int. Asia Conf. Inform. Control, Automat. Robot.*, vol. 3, no. 4, pp. 339–341, 2010.
- [19] "Chapter 3-thermo-optic coefficients," in *Handbook Optical Constants Solids*, E. D. Palik, Ed., Burlington: Acad. Press, 1997, pp. 115–261. [Online]. Available: <https://doi.org/10.1016/B978-012544415-6.50150-3>
- [20] G. Ghosh, "Temperature dispersion of refractive indexes in some silicate fiber glasses," *IEEE Photon. Technol. Lett.*, vol. 6, no. 3, pp. 431–433, Mar. 1994.
- [21] T. Goh, A. Himeno, M. Okuno, H. Takahashi, and K. Hattori, "High-extinction ratio and low-loss silica-based 8  $\times$  8 thermo-optic matrix switch," *IEEE Photon. Technol. Lett.*, vol. 10, no. 3, pp. 358–360, Mar. 1998.
- [22] B. Pan, F. Yan, X. Xue, E. Magelhaes, and N. Calabretta, "Performance assessment of a fast optical add-drop multiplexer-based metro access network with edge computing," *J. Opt. Commun. Netw.*, vol. 11, no. 12, pp. 636–646, 2019.
- [23] A. Alvarado, E. Agrell, D. Lavery, R. Maher, and P. Bayvel, "Replacing the soft-decision FEC limit paradigm in the design of optical communication systems," *J. Lightw. Technol.*, vol. 34, no. 2, pp. 707–721, 2016.
- [24] A. Alvarado, T. Fehenberger, B. Chen, and F. M. J. Willems, "Achievable information rates for fiber optics: Applications and computations," *J. Lightw. Technol.*, vol. 36, no. 2, pp. 424–439, 2018.
- [25] C. Pulikkaseril, L. A. Stewart, M. A. F. Roelens, G. W. Baxter, S. Poole, and S. Frisken, "Spectral modeling of channel band shapes in wavelength selective switches," *Opt. Exp.*, vol. 19, no. 9, pp. 8458–8470, 2011.
- [26] K. Okamoto, "16-channel optical add/drop multiplexer consisting of arrayed-waveguide gratings and double-gate switches," *Electron. Lett.*, vol. 32, no. 16, pp. 1471–1472, Aug. 1996.
- [27] A. Rigny, A. Bruno, and H. Sik, "Multigrating method for flattened spectral response wavelength multi/demultiplexer," *Electron. Lett.*, vol. 33, no. 20, pp. 1701–1702, 1997.
- [28] A. Gholipour and R. Faraji-Dana, "Nonuniform arrayed waveguide gratings for flat-top passband transfer function," *J. Lightw. Technol.*, vol. 25, no. 12, pp. 3678–3685, 2007.
- [29] S. Tsunashima *et al.*, "Silica-based, compact and variable-optical-attenuator integrated coherent receiver with stable optoelectronic coupling system," *Opt. Exp.*, vol. 20, no. 24, pp. 27174–27179, Nov. 2012.